Advanced Grid Synchronization Scheme Based on Dual eSOGI-FLL for Grid-Feeding Converters

Anh Tan Nguyen, *Member, IEEE*, and Dong-Choon Lee, *Senior Member, IEEE*

***Abstract*—In this article, an improved grid synchronization method for three-phase grid-feeding converters using a dual enhanced second-order generalized integrator (eSOGI) frequency-locked loop (FLL) is proposed. The eSOGI, of which gains can be adjusted based on the positive-sequence component of the grid voltage, is designed to estimate the grid voltage accurately. Moreover, to improve the grid frequency estimation under grid voltage sags, frequency rate limits is suggested in the FLL structure. The selection of the eSOGI-FLL parameters is described as well. After the estimated grid voltages are obtained using the dual eSOGI-FLL, they are used to synthesize the references in the dual-current controllers for positive- and negative-sequence components. Through the simulation and experimental results under grid voltage sags and distorted grid conditions, the improved power control performance of the proposed method has been demonstrated in comparison with those of the existing methods.**

***Index Terms*—Enhanced second-order generalized integrator (eSOGI), frequency-locked loop (FLL), grid faults, grid synchronization, power control.**

I. INTRODUCTION

RENEWABLE energy sources have received considerable attention in recent times due to global climate change and the exhaustion of fossil fuels. However, with the increased penetration of renewable energy into the grid, the grid inertia may reduce. Consequently, several grid problems, such as grid unbalance, distortion, frequency change, or even voltage sags, may arise.

Renewable energy systems are usually interfaced with the grid through power electronics converters, which not only deliver power to the grid but also provide a satisfactory performance under grid faults complying with the grid code requirements. To fulfill these goals, one of the most important control issues of grid-connected converters is grid synchronization, by which the electrical quantities of the grid, such as voltage, frequency, and phase angle, can be estimated.

Synchronous-reference-frame-based phase-locked loops (SRF-PLLs) have been conventionally applied for grid synchronization in three-phase systems owing to their simple implementation [1], [2]. However, their performance is not satisfactory under unbalanced grid conditions because of the existence of negative-sequence components of the grid voltage. Accordingly, improved PLL systems have been studied to overcome these limitations [3]–[10]. An improved PLL with simple implementation based on the concept of variable sampling frequency has been suggested [3]. However, since the PLL is only a small part of a large system in which the selection of sampling frequency is decided by many factors, hence the use of PLL with variable sampling frequency is not always possible [4], [5]. Delayed-signal-cancellation-based SRF-PLL using all-pass filters [6] and adaptive notch filters [7] have been studied for the extraction of the positive-sequence components of the grid voltage. Moreover, the decoupled double SRF-PLL [8] and moving-average-filter-based SRF-PLL [9], [10] have been suggested to mitigate the adverse effects of the negative-sequence components of the voltage on the grid synchronization performance.

Recently, owing to their simple structure and excellent harmonic rejection capability, second-order generalized integrator (SOGI) frequency-locked loop (FLL) structures have been widely applied to both grid-connected [11]–[13] and machine drive systems [14], [15]. In steady-state operations, the outputs of the SOGI-FLL structure are the estimated frequency and the in-phase and quadrature components, x' and qx', of its input x. Single SOGIs can be connected in series, that is, cascaded SOGI structure [16], or in parallel, that is, multi-SOGI structure [17] to improve the harmonic rejection capability. For grid synchronization, although the dual SOGI-FLL has been successfully applied to extract the positive- and negative-sequence components of grid voltage [18], its estimation speed is relatively low, as the SOGI gain is commonly limited to less than two. This may exacerbate the grid-side power fluctuations under grid fault events. Accordingly, the SOGI-FLL variants, whose gains can be arbitrarily selected, have been suggested to improve the estimation speed [19]–[22]. In the all-pass filter (APF) FLL, an APF is used for the quadrature component estimation [19]. Hence, the difference between the outputs due to the low subharmonic/dc offset can be eliminated. The steady-state linear Kalman filter (SSLKF) FLL [20], [21] and modified SOGI (mSOGI) modified FLL (mFLL) [22] have similar structures, where the qx' is estimated based on both x' and the error between x and x'. However, the harmonic rejection capability of these

Manuscript received June 13, 2021; revised November 5, 2021; accepted December 27, 2021. Date of publication January 6, 2022; date of current version February 18, 2022. This work was supported by the National Research Foundation of Korea Grant funded by the Korea Government (MSIT) under Grant 2021R1A2C2005996. Recommended for publication by Associate Editor Y. A.-R. I. Mohamed. *(Corresponding author: Dong-Choon Lee.)*

Anh Tan Nguyen is with the School of Electrical Engineering, Hanoi University of Science and Technology, Hai Ba Trung 100000, Vietnam (e-mail: nguyenanhtan91bk@gmail.com).

Dong-Choon Lee is with the Department of Electrical Engineering, Yeungnam University, Gyeongbuk 38541, South Korea (e-mail: dclee@yu.ac.kr).

Color versions of one or more figures in this article are available at https://doi.org/10.1109/TPEL.2022.3140893.

Digital Object Identifier 10.1109/TPEL.2022.3140893

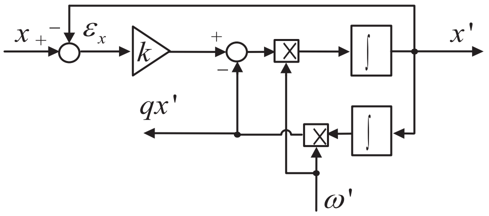

Fig. 1. Standard SOGI structure.

SOGI-FLL variants is deteriorated substantially compared with that of the SOGI. Therefore, a structure in which single mSOGIs are connected in parallel is recommended to eliminate the specified harmonics in its output. However, this structure can cause a high computational burden. Recently, the enhanced FLL (eFLL) has been suggested as well [23]. In eFLL, instead of only using the integral term, the proportional term is used in combination with the integral term to improve the grid frequency estimation. However, the eFLL has almost no significant impact on the estimation of positive- and negative-sequence components of grid voltage.

This article proposes a novel grid synchronization control method for three-phase grid-connected converters using a dual enhanced SOGI (eSOGI) FLL. The eSOGI gains can be adjusted based on the value of the positive-sequence components of the grid voltage, whereas the frequency rate limit is included in the FLL structure. With the proposed method, the grid voltages can be accurately estimated even under grid faults. Then, the positive- and negative-sequence components of the grid current references are synthesized. Consequently, the grid-side power control performance can be improved compared with that of the existing methods. The feasibility of the proposed method is confirmed through simulation and experimental results under grid voltage sags and distorted conditions.

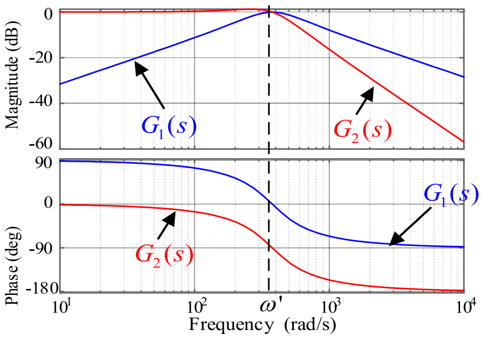

Fig. 2. Bode plots of SOGI transfer functions.

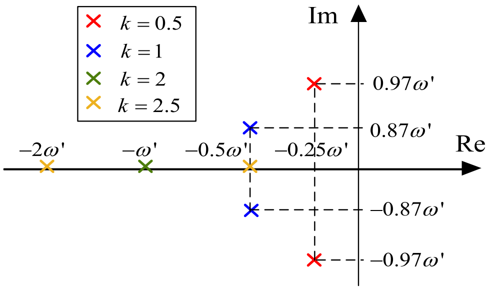

Fig. 3. Root loci of SOGI.

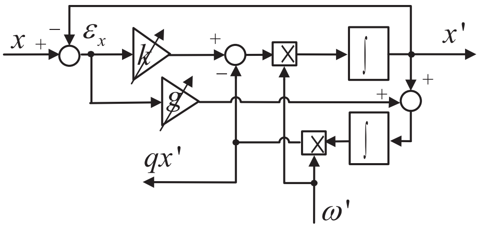

Fig. 4. Enhanced SOGI structure.

II. Structure of Standard SOGI

Fig. 1 shows the structure of the standard SOGI, in which x is the input signal, x' and qx' are the output signals, k is the SOGI gain, and ω' is the tuning frequency. The transfer functions of the SOGI are expressed as [18]

$$G_1(s) = \frac{x'(s)}{x(s)} = \frac{k\omega' s}{s^2 + sk\omega' + \omega'^2} \tag{1}$$

$$G_2(s) = \frac{qx'(s)}{x(s)} = \frac{k\omega'^2}{s^2 + sk\omega' + \omega'^2}. \tag{2}$$

For example, with $k = 1$ and $\omega' = 2\pi 60$ rad/s, the Bode plots of the SOGI transfer functions are shown in Fig. 2. If ω' is close to ω, then x' and qx' approximate the in-phase and quadrature components of x, respectively. Notably, as $G_1(s)$ and $G_2(s)$ behave like band-pass and low-pass filters, respectively, the negative effects of the harmonics in x on x' and qx' can be significantly reduced.

Fig. 3 shows the root loci of the SOGI under manifold conditions of k. It is observed that the fastest response of the SOGI is achieved when $k = 2$ is applied. However, for a satisfactory compromise between the dynamic response and overshoot, k is commonly set to 1 [24], [25] or $\sqrt{2}$ [15], [18].

III. Proposed Dual Enhanced SOGI-FLL Structure

A. Dual eSOGI-FLL for Grid Voltage Estimation

Under grid fault conditions, an incorrect estimation of grid voltages, from which the grid angle and the synthesized grid current references are obtained, may exacerbate the fluctuations of the grid-side powers [26]. In this article, a grid voltage estimation by applying the dual eSOGI-FLL is proposed to overcome these difficulties.

Compared with the standard SOGI, a variable gain g is added to the eSOGI, as shown in Fig. 4. This gain can provide the required degree of freedom to improve the transient performance of the eSOGI [22]. The values of k and g are adjusted based on the amplitude of estimated positive-sequence component of the grid voltage $\hat{E}^+$ and threshold δ, as follows:

$$k = \begin{cases} k_{\text{normal}}, & \left(d\hat{E}^+ \big/ dt\right) < \delta \\ k_{\text{fault}}, & \left(d\hat{E}^+ \big/ dt\right) \geq \delta \end{cases} \tag{3}$$

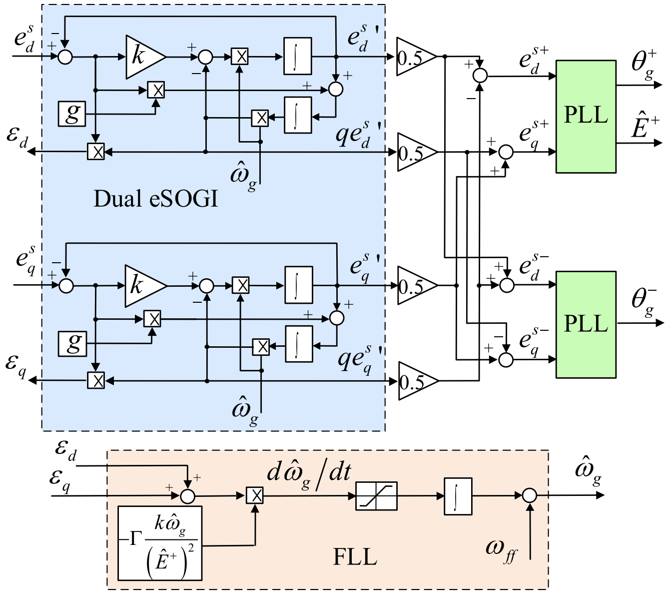

Fig. 5. Dual eSOGI-FLL-PLL structure for grid synchronization.

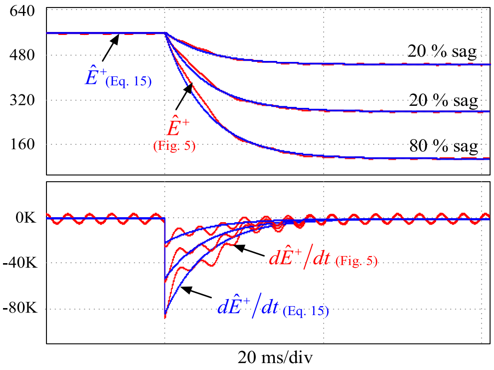

Fig. 6. Grid voltage estimation performance under various voltage sags. (a) Values of $\hat{E}^+$(V). (b) Derivatives of $\hat{E}^+$(V/s).

$$g = \begin{cases} 0, & \left(d\hat{E}^+ \big/ dt\right) < \delta \\ g_{\text{fault}}, & \left(d\hat{E}^+ \big/ dt\right) \geq \delta \end{cases} \tag{4}$$

where k_{normal}, k_{fault}, and g_{fault} are constants, and k_{fault} is larger than k_{normal}. The symbol "^" is used to denote the estimated value. The superscript "+" represents the positive-sequence component. The letter "d" indicates a derivative. The dual eSOGI-FLL-PLL structure for the grid voltage estimation is shown in Fig. 5, in which the grid frequency ω_g is estimated by the FLL, and the positive- and negative-sequence components of the grid voltages, e_{dq}^{s+} and e_{dq}^{s-}, are obtained as

$$e_d^{s+} = 0.5\left(e_d^s{}' - qe_q^s{}'\right) \tag{5}$$

$$e_q^{s+} = 0.5\left(qe_d^s{}' + e_q^s{}'\right) \tag{6}$$

$$e_d^{s-} = 0.5\left(e_d^s{}' + qe_q^s{}'\right) \tag{7}$$

$$e_q^{s-} = 0.5\left(-qe_d^s{}' + e_q^s{}'\right) \tag{8}$$

where the superscript "-" represents the negative-sequence component and $qe_{dq}^s{}'$ represents the quadrature components of $e_{dq}^s{}'$.

B. Determination of eSOGI Parameters

The transfer functions of the eSOGI in Fig. 5 are expressed as

$$\frac{e_d^s{}'(s)}{e_d^s(s)} = \frac{k\hat{\omega}_g s - g\hat{\omega}_g^2}{s^2 + k\hat{\omega}_g s + (1-g)\,\hat{\omega}_g^2} \tag{9}$$

$$\frac{qe_d^s{}'(s)}{e_d^s(s)} = \frac{k\hat{\omega}_g^2 + g\hat{\omega}_g s}{s^2 + k\hat{\omega}_g s + (1-g)\,\hat{\omega}_g^2}. \tag{10}$$

Assuming that $e_d^s = A\cos(\omega_g t) + \sum_{h=2}^{\infty} A_h \cos(\omega_h t)$ and $e_q^s = A\sin(\omega_g t) + \sum_{h=2}^{\infty} A_h \sin(\omega_h t)$ in which h represents the harmonic order and $\omega_h = h\omega_g$, the outputs $e_d^s{}'$, $qe_d^s{}'$, $e_q^s{}'$ and $qe_q^s{}'$ are derived under steady-state operation from (9) and (10) as

$$e_d^s{}' = A\cos(\omega_g t) + \sum_{h=2}^{\infty} H_h \cos\left(\omega_h t + \operatorname{atan}(\Phi_h)\right) \tag{11}$$

$$qe_d^s{}' = A\sin(\omega_g t) + \sum_{h=2}^{\infty} H_{qh} \sin\left(\omega_h t + \operatorname{atan}(\Phi_{qh})\right) \tag{12}$$

$$e_q^s{}' = A\sin(\omega_g t) + \sum_{h=2}^{\infty} H_h \sin\left(\omega_h t + \operatorname{atan}(\Phi_h)\right) \tag{13}$$

$$qe_q^s{}' = -A\cos(\omega_g t) - \sum_{h=2}^{\infty} H_{qh} \cos\left(\omega_h t + \operatorname{atan}(\Phi_{qh})\right) \tag{14}$$

where

$$H_h = A_h\omega_g \sqrt{\frac{(k\omega_h)^2 + (g\omega_g)^2}{(k\omega_h\omega_g)^2 + \left(\omega_g^2 - \omega_h^2 - g\omega_g^2\right)^2}}$$

$$\Phi_h = \frac{k\omega_h\left(\omega_g^2 - \omega_h^2\right)}{k^2\omega_h^2\omega_g - g\omega_g\left(\omega_g^2 - \omega_h^2 - g\omega_g^2\right)}$$

$$H_{qh} = A_h\omega_g \sqrt{\frac{(k\omega_g)^2 + (g\omega_h)^2}{(k\omega_h\omega_g)^2 + \left(\omega_g^2 - \omega_h^2 - g\omega_g^2\right)^2}}$$

$$\Phi_{qh} = \frac{k\omega_g\left(\omega_g^2 - \omega_h^2 - g\omega_g^2 + g\omega_h^2\right)}{k^2\omega_h\omega_g^2 + g\omega_h\left(\omega_h^2 - \omega_g^2 + g\omega_g^2\right)}.$$

From (11)–(14), large harmonics may exist in the estimated positive- and negative-sequence components under distorted grid conditions if a high value of g is applied. Therefore, to reduce the adverse effects of grid voltage harmonics, g must be set to zero under these conditions by appropriately selecting δ in (4).

Under grid voltage sags in which E^+ is reduced from the nominal value E_0 to the fault value E_{sag}, assuming that k and g are set to 1 and 0, respectively, and $\hat{\omega}_g$ is locked to the grid frequency of $2\pi 60$ rad/s, $\hat{E}^+$ at fault occurrence can be approximated as

$$\begin{aligned} \hat{E}^+ &\approx \left(E_0 - E_{\text{sag}}\right) e^{-(k\hat{\omega}_g t)/2} + E_{\text{sag}} \\ &\approx \left(E_0 - E_{\text{sag}}\right) e^{-60\pi t} + E_{\text{sag}}. \end{aligned} \tag{15}$$

Under various grid voltage sags, Fig. 6(a) illustrates the voltage amplitudes $\hat{E}^+$obtained by the proposed structure shown in

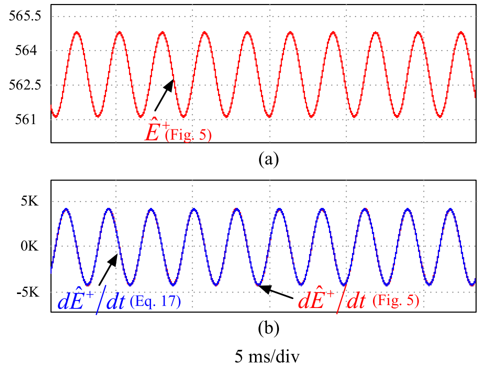

Fig. 7. Grid voltage estimation performance under distorted grid condition. (a) Value of $\hat{E}^+$(V). (b) Derivative of $\hat{E}^+$(V/s).

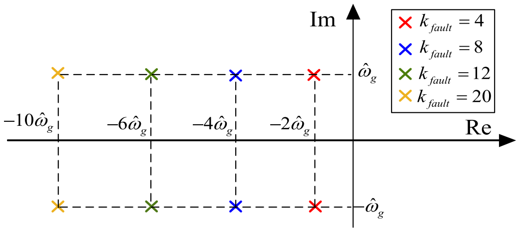

Fig. 8. Root loci of eSOGI.

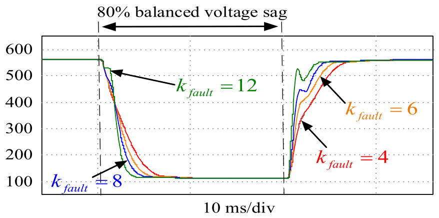

Fig. 9. Estimation performance of $\hat{E}^+$under 80% balanced sag.

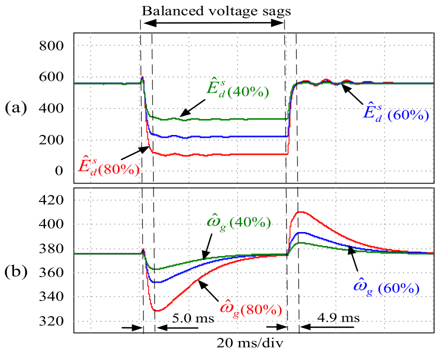

Fig. 10. Estimation performance under various balanced sags. (a)$\hat{E}^s_d$(V). (b) $\hat{\omega}_g$ (rad/s).

Fig. 5 with 8% fifth- and 4% seventh-order harmonic components of grid voltage and theoretically calculated using (15) without considering the harmonic components; Fig. 6(b) shows the derivatives of $\hat{E}^+$. It is observed that the amplitudes $\hat{E}^+$obtained from Fig. 5 and (15) are similar to each other in terms of the settling times and the maximum values of $d\hat{E}^+/dt$. Therefore, it is worth mentioning that the feasibility of (15) is confirmed, and the maximum values of the derivatives of $\hat{E}^+$in (15) is not significantly affected by the harmonic components of the grid voltage. Accordingly, based these maximum values of $d\hat{E}^+/dt$, the following selection of δ can allow the determinations of k and g in (3) and (4), respectively, not to be adversely affected by the harmonic components under various grid voltage sags.

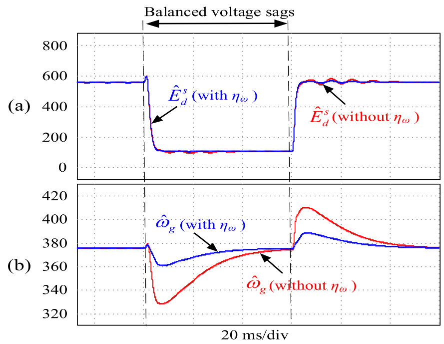

Fig. 11. Estimation performance with and without η_ω under 80% balanced sag. (a)$\hat{E}^s_d$(V). (b) $\hat{\omega}_g$ (rad/s).

If k_{normal} of eSOGI is set to 1, similar to that of SOGI, δ can be selected based on (15) as

$$\delta = k_\delta \times |(E_0 - E_{\text{sag}})\,k_{\text{normal}}\omega_g|/2 \tag{16}$$

where $|((E_0 - E_{\text{sag}})k_{\text{normal}}\omega_g)/2|$represents the maximum value of $d\hat{E}^+/dt$; k_δ is a constant which is slightly less than one, e.g., 0.8; if grid voltage amplitudes below 0.85 p.u. are considered as low-voltage faults, E_{sag} is set to 85% of E_0. Notably, the existence of k_δ in (16) is required to ensure $(d\hat{E}^+/dt) \geq \delta$ under fault events.

Under the distorted grid conditions, the derivative of voltage amplitude $\hat{E}^+$ can be expressed based on (11)–(14) as

$$\begin{aligned}\frac{d\hat{E}^+}{dt} = {} & \Bigg[2A\cos(\omega_g t) + \sum_{h=2}^{\infty}\Bigg(H_h\cos(\omega_h t + \text{atan}\Phi_h) \\ & + H_{qh}\cos(\omega_h t + \text{atan}\Phi_{qh})\Bigg)\Bigg] \times \Bigg[-2A\omega_g\sin(\omega_g t) \\ & - \sum_{h=2}^{\infty}\omega_h\left(H_h\sin(\omega_h t + \text{atan}\Phi_h) + H_{qh}\sin(\omega_h t\right. \\ & \left. +\text{atan}\Phi_{qh})\right)\Bigg] \Bigg/ 4\hat{E}^+ \\ & + \Bigg[2A\sin(\omega_g t) + \sum_{h=2}^{\infty}\left(H_{qh}\sin(\omega_h t + \text{atan}\Phi_{qh})\right. \\ & \left. + H_h\sin(\omega_h t + \text{atan}\Phi_h)\right)\Bigg] \times \Bigg[2A\omega_g\cos(\omega_g t) \\ & + \sum_{h=2}^{\infty}\omega_h\left(H_{qh}\cos(\omega_h t + \text{atan}\Phi_{qh}) + H_h\cos(\omega_h t\right. \\ & \left. +\text{atan}\Phi_h)\right)\Bigg] \Bigg/ 4\hat{E}^+\end{aligned} \tag{17}$$

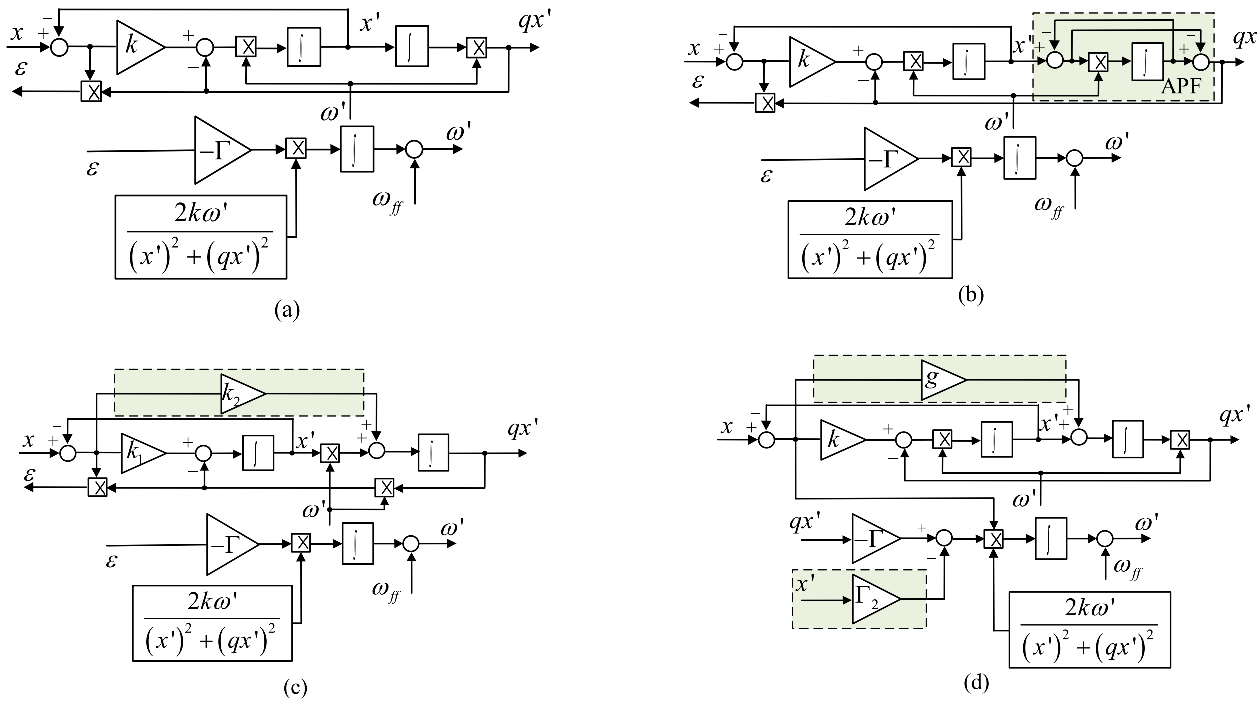

(a) (b) (c) (d)

Fig. 12. SOGI-FLL and its variants. (a) Second-order generalized integrator -FLL. (b) All-pass filter FLL. (c) Steady-state linear Kalman filter FLL. (d) mSOGI-mFLL.

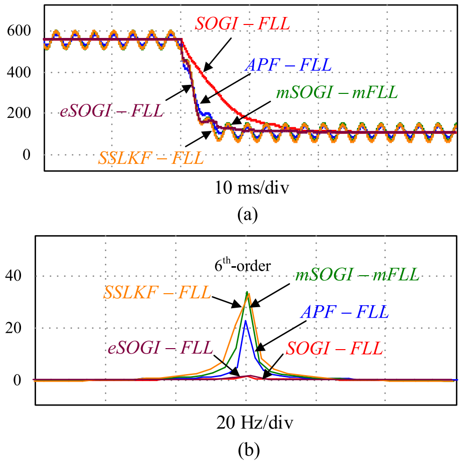

(a)

(b)

Fig. 13. Grid voltage estimation performance under 80% balanced sag and distorted grid conditions. (a) $\hat{E}^+$ (V). (b) Harmonic spectra of $\hat{E}^+$(V).

From (17), the maximum value of $d\hat{E}^+/dt$ can be theoretically obtained under various distorted grid conditions. The information of maximum value of $d\hat{E}^+/dt$ is very meaningful to the proposed method since it can show whether the values of k and g vary under distorted grid conditions.

Fig. 7 shows $\hat{E}^+$ and its derivatives in presence of 8% fifth- and 4% seventh-order harmonic components included in the grid voltage. In Fig. 7(b), the red line is obtained from Fig. 5, whereas the blue line is obtained from (17). Then, it can be confirmed that the validity of (17) is verified. In Fig. 7(b), the maximum value of $d\hat{E}^+/dt$ is about 4100, and it is less than the threshold δ selected as 12 700 by (16), hence k and g can be maintained at k_{normal} and zero under this condition. As a result, the adverse effects of harmonics on the grid voltage estimation can be significantly mitigated, as shown in (11)–(14).

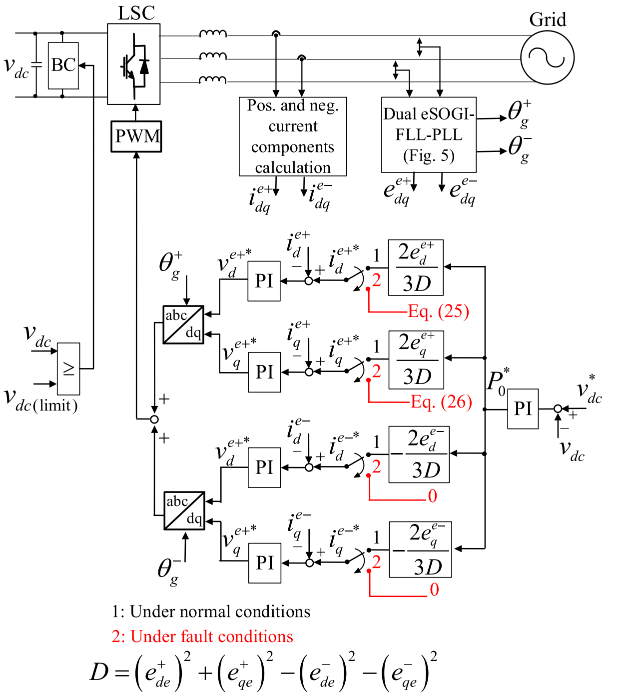

Fig. 14. Line-side converter control configuration.

With δ in (16), assuming that g and k are set to g_{fault} and k_{fault}, respectively, under grid voltage sags owing to (3) and (4),

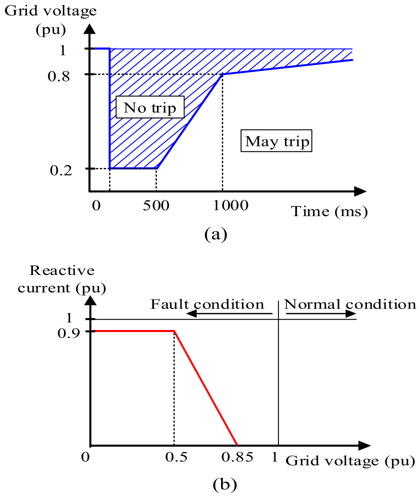

Fig. 15. Grid code [31]. (a) Low-voltage ride-through requirement. (b) Reactive current requirement.

the poles of the transfer functions (9) and (10) are solved as

$$s_{1,2} = -k_E\hat{\omega}_g/2 \pm \hat{\omega}_g\sqrt{k_{\text{fault}}^2 - 4\left(1 - g_{\text{fault}}\right)}\Big/2. \quad (18)$$

If g_{fault} is chosen as

$$g_{\text{fault}} = -k_{\text{fault}}^2/4 \quad (19)$$

the poles $s_{1,\,2}$ in (18) are rewritten as

$$s_{1,2} = -k_{\text{fault}}\hat{\omega}_g/2 \pm j\hat{\omega}_g. \quad (20)$$

The root loci of the eSOGI based on (21) are shown in Fig. 8. Since $s_{1,\,2}$ are always located on the left-half plane, the stability of the eSOGI is guaranteed. Moreover, with the real parts of $s_{1,\,2}$ of $-k_{\text{fault}}\hat{\omega}_g/2$, the settling time of the eSOGI response can be approximated as

$$t_{s(\text{eSOGI})} \approx 10/k_{\text{fault}}\hat{\omega}_g. \quad (21)$$

It is noted that although k_{fault} can be arbitrarily selected to achieve the pre-specified settling time in (21), it should be limited to avoid the high fluctuations in $\hat{E}^+$ at fault occurrence and clearance.

Fig. 9 shows the $\hat{E}^+$ estimation performance under 80% balanced sag with various values of k_{fault}. For simplification, it is assumed that $\hat{\omega}_g$ is locked to the grid frequency of 2π60 rad/s. As shown in Fig. 9, the higher values of k_{fault} correspond to faster settling of the $\hat{E}^+$ estimation system as aforementioned in (21). However, higher fluctuations of $\hat{E}^+$can be observed as well. Therefore, for a satisfactory compromise between the dynamic response and the fluctuation, $k_{\text{fault}} = 6$ and then $g_{\text{fault}} = -9$ according to (19) are selected in this article.

C. Determination of Frequency Rate Limit in FLL

Assuming that the signal $d\hat{\omega}_g/dt$ of the FLL in Fig. 5 is not limited, and $k_{\text{fault}} = 6$, $g_{\text{fault}} = -9$ and $\Gamma = 25$ corresponding to $t_{s(FLL)}$ of 100 ms [18] are selected, then Fig. 10 shows the estimation performances of $\hat{E}_d^s = \sqrt{({e_d^s}')^2 + ({qe_d^s}')^2}$ and $\hat{\omega}_g$under various grid voltage sags. In Fig. 10, owing to the large frequency estimation errors $\Delta\omega_g$, large fluctuations in $\hat{E}_d^s$ exist after fault clearance. Therefore, to reduce these adverse effects, $d\hat{\omega}_g/dt$needs to be limited.

From Fig. 10, after fault occurrence and clearance, the times for $\hat{\omega}_g$ to change near-linearly before reaching the minimum and maximum values are approximately the eSOGI settling time $t_{s(\text{eSOGI})}$ in (21), i.e., 4.4 ms. Thus, if the frequency estimation error limit $\Delta\omega_{g(\text{limit})}$ under these conditions is prespecified, the limit value η_ω of $|d\hat{\omega}_g/dt|$can be determined based on (21) and $\Delta\omega_{g(\text{limit})}$ as

$$\eta_\omega = \Delta\omega_{g(\text{limit})}\big/t_{s(\text{eSOGI})} = \Delta\omega_{g(\text{limit})}k_{\text{fault}}\omega_g\big/10. \quad (22)$$

For example, with $\Delta\omega_{g(\text{limit})} = 20$ rad/s, $k_{\text{fault}} = 6$, and $\omega_g = 2\pi 60$ rad/s, η_ω can be selected as 4500 from (22). Fig. 11 shows the estimation performances of $\hat{E}_d^s$ and $\hat{\omega}_g$under an 80% balanced voltage sag with and without η_ω. As shown in Fig. 11, without η_ω, the fluctuations of $\hat{E}_d^s$ and $\Delta\omega_g$ are about 37.8 V and 34.5 rad/s, respectively, after fault clearance. On the other hand, with η_ω added, they are only 13.6 V and 13.1 rad/s, respectively. It is noted from (22) that although η_ω can be arbitrarily selected to achieve the pre-specified low error $\Delta\omega_{g(\text{limit})}$, this can slow down the frequency estimation of the FLL under the grid frequency variations. Therefore, lower limit of η_ω has to be considered as well. Assuming that the time constant of the FLL is 1/(2Γ) [27], and the transient response of $\hat{\omega}_g$ is in the form of an exponential curve [18], the maximum value of $d\hat{\omega}_g/dt$ under grid frequency variations is approximated as $2\Gamma\Delta_\omega$, in which Δ_ω represents the frequency variation specified in the grid code requirements. Therefore, the lower limit of η_ω can be determined without having any negative effects on the estimation performance of the FLL as

$$\eta_\omega > 2\Gamma\Delta_\omega. \quad (23)$$

For example, with $\Delta_\omega = 31.4$ rad/s (5 Hz) [28], $\eta_\omega > 1570$ is calculated using (23). Thus, the aforementioned selection of η_ω of 4500 is reasonable.

D. Estimation Performance of Positive-Sequence Component of Grid Voltage

Fig. 12 shows the structures of SOGI-FLL, APF-FLL, SSLKF-FLL, and mSOGI-mFLL. Under 80% balanced voltage sag and distorted grid condition with 8% fifth- and 4% seventh-order harmonics in the grid voltage, the performances of grid voltage estimation using dual SOGI-FLL, dual APF-FLL, dual SSLKF-FLL, dual mSOGI-mFLL, and dual eSOGI-FLL are shown in Fig. 13. It is assumed that ω' is locked to the grid frequency of 2 π60 rad/s. The gains of the SOGI-FLL, the APF-FLL, the SSLKF-FLL, the mSOGI-mFLL, and the eSOGI-FLL are selected as follows:

$$\text{SOGI} - \text{FLL} : k = 1;$$

$$\text{APF} - \text{FLL} : k = 6;$$

$$\text{SSLKF} - \text{FLL} : k_1 = 2263 \,\text{and}\, k_2 = -3393;$$

$$m\text{SOGI} - m\text{FLL} : k = 6 \,\text{and}\, g = -9;$$

$$\text{eSOGI} - \text{FLL} : k_{\text{normal}} = 1, k_{\text{fault}} = 6, g_{\text{fault}} = -9 \,\text{and}\, \delta = 12700.$$

In Fig. 13, the settling times of APF-FLL, SSLKF-FLL, and mSOGI-mFLL are similar to each other, and they are faster than that of SOGI-FLL. However, the harmonic rejection capabilities of APF-FLL, SSLKF-FLL and mSOGI-mFLL are significantly deteriorated in this case, and hence the sixth-order harmonic amplitude of $\hat{E}^{+}$ using these structure are quite large, i.e., 23, 34, and 34 V, respectively, as shown in Fig. 13(b). It is observed from Fig. 13, the proposed eSOGI-FLL can provide the superior performance with short estimation time (about 5 ms) and low harmonic amplitude (about 2 V).

IV. CONTROL OF GRID-FEEDING CONVERTER

Fig. 14 shows the control configuration of the grid-feeding converter. The positive- and negative-sequence components of the grid voltages are extracted by the proposed dual eSOGI-FLL structure shown in Fig. 5, while the positive- and negative-sequence components of grid currents are extracted by delayed signal cancellation method [29] using the first-order all-pass filters. The dc-link voltage is controlled by adjusting the active power reference P_0^*. Under normal grid conditions, the grid-side reactive power is controlled to zero for unity power factor operation. To eliminate the double-grid- frequency dc-link voltage ripples in the case of an unbalanced grid, dual-current controllers for positive- and negative-sequence components are utilized. Then, the grid current references are derived as [30]

$$\begin{bmatrix} i_d^{e+*} \\ i_q^{e+*} \\ i_d^{e-*} \\ i_q^{e-*} \end{bmatrix} = \begin{bmatrix} e_d^{e+} e_q^{e+} e_d^{e-} e_q^{e-} \\ e_q^{e+} - e_d^{e+} e_q^{e-} - e_d^{e-} \\ e_q^{e-} - e_d^{e-} - e_q^{e+} e_d^{e+} \\ e_d^{e-} e_q^{e-} e_d^{e+} e_q^{e+} \end{bmatrix}^{-1} \begin{bmatrix} 2P_0^*/3 \\ 0 \\ 0 \\ 0 \end{bmatrix}$$

$$= \frac{2P_0^*}{3D} \begin{bmatrix} e_d^{e+} \\ e_q^{e+} \\ -e_d^{e-} \\ -e_q^{e-} \end{bmatrix} \tag{24}$$

where $D = [(e_d^{e+})^2 + (e_q^{e+})^2] - [(e_d^{e-})^2 + (e_q^{e-})^2]$.

The Spanish grid code for the fault ride-through requirements [31] is shown in Fig. 15. Thus, under grid voltage sags, the current referencei_d^{e+*} is set according to the grid voltage amplitude as

$$\begin{cases} i_d^{e+*} = -0.9, if 0 \leq \hat{E}^{+} \leq 0.5(\text{p.u.}) \\ i_d^{e+*} = -2.186 + 2.571 \times \hat{E}^{+}, if 0.5 < \hat{E}^{+} \leq 0.85(\text{p.u.}) \\ i_d^{e+*} = 0, if \hat{E}^{+} > 0.85(\text{p.u.}). \end{cases} \tag{25}$$

Simultaneously, i_d^{e-} and i_q^{e-} are controlled to zero, and $i_q^{e+*}$is obtained as

$$i_q^{e+*} = 2P_0^*/3e_q^{e+}. \tag{26}$$

It is worth mentioning that i_q^{e+*}in (26) needs to be limited as $|i_q^{e+*}| \leq \sqrt{i_{\text{rated}}^2 - i_d^{e+*}}$so that the grid current reference does not exceed the rated value i_{rated}. Moreover, since the current references in (24)–(26) are functions of the estimated grid voltages, the accurate estimation of grid voltages is essential to achieve the desired control performance. In Fig. 14, the braking resistor should be activated if the dc-link voltage exceeds the prespecified limit.

V. SIMULATION RESULTS

The simulation of the proposed method applied to a 2-MW Squirrel-cage induction generator (SCIG) wind turbine system was performed using the PSIM platform. The grid voltage is 690 V/60 Hz. The dc-link voltage is controlled at 1200 V. The sampling time is 0.1 ms. The switching frequency is 5 kHz. The dual eSOGI-FLL parameters were selected as follows, as mentioned earlier: $k_{\text{normal}} = 1$; $k_{\text{fault}} = 6$; $g_{\text{fault}} = -9$; $\delta = 12700$; and $\eta_\omega = 4500$. The PLL parameters are designed based on the symmetrical optimum method [2] with a crossover frequency of 80 Hz.

It can be noted from Fig. 13(a) that under 80% balanced voltage sag, since the settling times of eSOGI response and mSOGI response are similar to each other, the estimated grid angles as well as the positive- and negative-sequence components of the grid current references obtained using the proposed method and the mSOGI-mFLL-based synchronization method are similar to each other. Consequently, under this condition, there is not significant difference between the grid-side power control performances obtained using the proposed method and the mSOGI-mFLL-based synchronization method.

Although the mSOGI can give the fast response when its gains are high sufficiently, its harmonic rejection capability is deteriorated, as shown in Fig. 13. This adverse effect can be reduced when the mSOGI gains are low sufficiently, e.g., $k_{(m\text{SOGI})} = 1$ and $g_{(m\text{SOGI})} = -1/4$. However, this increases the settling time of mSOGI response $t_{s(m\text{SOGI})}$ owing to $t_{s(m\text{SOGI})} \approx 10/k_{(m\text{SOGI})}\hat{\omega}_g$. Moreover, the outputs of mSOGI with $k_{(m\text{SOGI})} = 1$ have the higher harmonic components compared to those of the eSOGI with $k_{\text{normal}} = 1$ and the SOGI with $k_{(\text{SOGI})} = 1$. These increased settling time and increased harmonic components are the drawbacks of the mSOGI with low gains. Therefore, the mSOGI with high gains are usually used to achieve the fast settling time [22].

As mentioned in Introduction section, although the SOGI can give the excellent harmonic rejection capability, it cannot provide the accurate grid voltage estimation under voltage sags due to its limited gain.

Different from existing SOGI-FLL and its variants, the determination of eSOGI gains, k and g, based on $d\hat{E}^{+}/dt$ and δ is the key idea of the proposed method, as shown in (3) and (4). Accordingly, the proposed method can give the accurate grid voltage estimation under various grid conditions, e.g., grid voltage sags and distorted grid conditions. To clarify the outstanding advantages of the proposed method in comparison with the existing ones, the performance tests are conducted as follows.

1) The dual SOGI-FLL-based synchronization method and the proposed method are tested under balanced grid voltage sag.

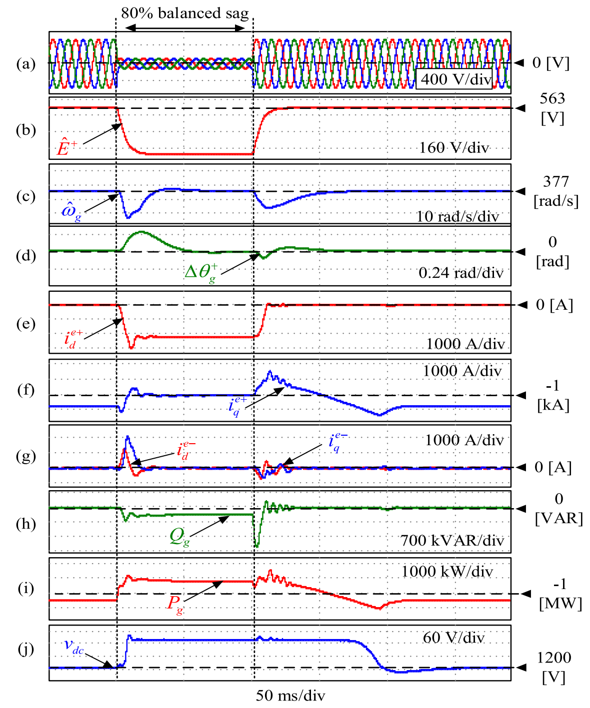

Fig. 16. System performance under 80% balanced sag using dual SOGI-FLL-based synchronization method. (a) Grid voltages (V). (b) $\hat{E}^+$(V). (c) $\hat{\omega}_g$(rad/s). (d) Phase angle estimation error (rad). (e) Positive-sequence d-axis grid current component (A). (f) Positive-sequence q-axis grid current component (A). (g) Negative-sequence grid current components (A). (h) Grid-side reactive power (VAR). (i) Grid-side active power (W). (j) DC-link voltage (V).

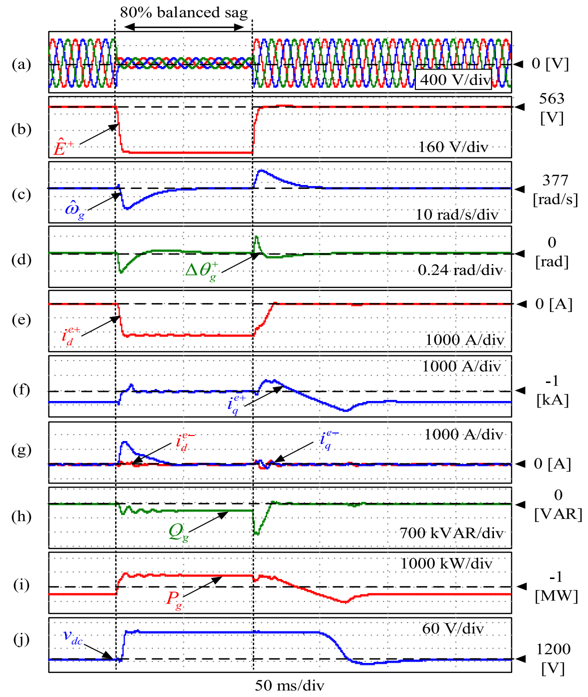

Fig. 17. System performance under 80% balanced sag using proposed method. (a) Grid voltages (V). (b) $\hat{E}^+$(V). (c) $\hat{\omega}_g$(rad/s). (d) Phase angle estimation error (rad). (e) Positive-sequence d-axis grid current component (A). (f) Positive-sequence q-axis grid current component (A). (g) Negative-sequence grid current components (A). (h) Grid-side reactive power (VAR). (i) Grid-side active power (W). (j) DC-link voltage (V).

2) The dual mSOGI-mFLL-based synchronization method and the proposed method are tested under distorted grid condition.

Fig. 16 shows the system performance when using the dual SOGI-FLL-based synchronization method under 80% balanced voltage sag. The grid-phase voltages are illustrated in Fig. 16(a). $\hat{E}^+$ and $\hat{\omega}_g$ are shown in Fig. 16(b) and (c), respectively. Fig. 16(d) shows the grid phase angle estimation error $\Delta\theta_g$. Under the fault event,i_d^{e+} is injected into the grid to support the grid voltage recovery [32], whereas i_q^{e+} is reduced to maintain the grid current amplitude at its rated value.i_d^{e-} and i_q^{e-} are controlled to zero as mentioned in Section IV. The dc-link voltage is limited to below 1350 V (112.5% of v_{dc}^*) by the breaking chopper system, as shown in Fig. 16(j).

The system performance of the proposed method under balanced voltage sag is shown in Fig. 17. In Fig. 17(a), the grid voltages are reduced in a manner similar to those in Fig. 16(a). It is observed that the synthesis of grid current references based on correctly estimated grid voltages can significantly reduce grid current fluctuations under fault events. As shown in Fig. 17(f), the current fluctuation Δi_q^{e+} with the proposed method is about 2068 A, but it is about 2980 A in Fig. 16(f) with the dual SOGI-FLL-based method. Moreover, Δi_d^{e-} and $\Delta i_q^{e-}$with the proposed method are only about 524 and 1609 A, respectively, as illustrated in Fig. 17(g). In contrast, they are about 1841 and 2259 A, respectively, with the dual SOGI-FLL-based method, as shown in Fig. 16(g). Fig. 17(h) and (i) shows that, with the proposed method, the power fluctuations after fault clearance, $\Delta P_{g(\text{clear})}$ and $\Delta Q_{g(\text{clear})}$, are about 1.73 MW and 1.59 MVAr, respectively. These fluctuations are lower than those with the existing method (2.61 MW for $\Delta P_{g(\text{clear})}$, 2.22 MVAr for $\Delta Q_{g(\text{clear})}$).

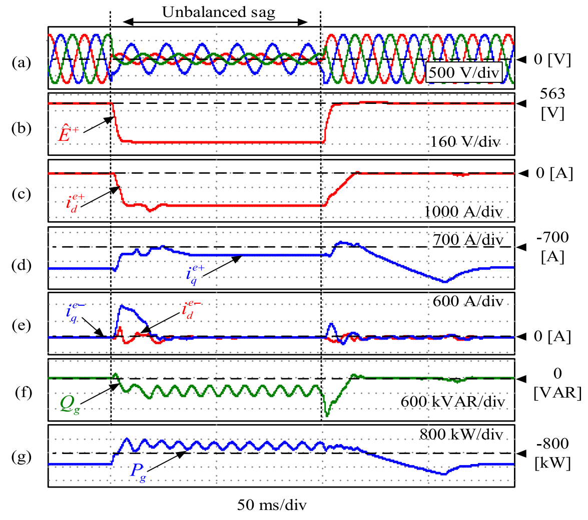

Fig. 18. System performance under unbalanced sag using proposed method. (a) Grid voltages (V). (b) $\hat{E}^+$(V). (c) Positive-sequence d-axis grid current component (A). (d) Positive-sequence q-axis grid current component (A). (e) Negative-sequence grid current components (A). (f) Grid-side reactive power (VAR). (g) Grid-side active power (W).

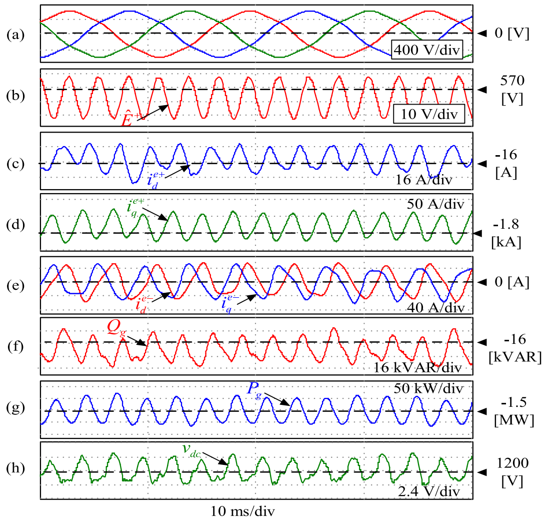

Fig. 19. System performance under distorted grid conditions using dual mSOGI-mFLL-based synchronization method. (a) Grid voltages (V). (b) $\hat{E}^+$(V). (c) Positive-sequence d-axis grid current component (A). (d) Positive-sequence q-axis grid current component (A). (e) Negative-sequence grid current components (A). (f) Grid-side reactive power (VAR). (g) Grid-side active power (W). (h) DC-link voltage (V).

Fig. 18 illustrates the system performance of the proposed method under unbalanced voltage sag. Similar to the balanced fault, during fault event, i_d^{e-} and i_q^{e-} are controlled to zero, i_d^{e+} is injected into the grid to support the grid recovery efforts, and $i_q^{e+}$is reduced to limit the grid current to the rated value. As shown in Fig. 18(f) and (g), the double-grid-frequency ripples in Q_g and P_g are caused by the negative-sequence components of the grid voltages.

Fig. 19 shows the system performance using the dual mSOGI-mFLL-based synchronization method under distorted grid conditions. The phase grid voltages, in which 4% fifth-order harmonics are included, and $\hat{E}^+$ are shown in Fig. 19(a) and (b). The currents i_d^{e+}, i_q^{e+}, i_d^{e-} and i_q^{e-} are controlled to their references obtained from(24). Fig. 19(g) shows that the reactive power is controlled to zero for a unity power factor operation.

The system performance of the proposed method under distorted grid condition is shown in Fig. 20, assuming 4% fifth-order grid voltage harmonics. As mentioned in Section III, as the eSOGI gains, k and g, are set to k_{normal} and zero, respectively, under this condition, the negative effects of the harmonics on the estimated grid voltages can be significantly mitigated, as shown by (11)–(14). Then, the synthesis of the grid current references based on the estimated grid voltages in (24) becomes robust against grid harmonics. In Fig. 20(c)–(e), the grid current fluctuations Δi_d^{e+}, Δi_q^{e+}, Δi_d^{e-} and $\Delta i_q^{e-}$with the proposed method are about 8, 8.8, 9.7, and 10.2 A, respectively. In contrast, with the dual mSOGI-mFLL-based method, they are about 42.5, 94.6, 113.2, and 115.5 A, respectively, as shown in Fig. 19(c)–(e). As a result, the power fluctuations with the proposed method (60.3 kW for ΔP_g) shown in Fig. 20(g) are lower than those with the dual mSOGI-mFLL-based method (140.2 kW for ΔP_g) shown in Fig. 19(g).

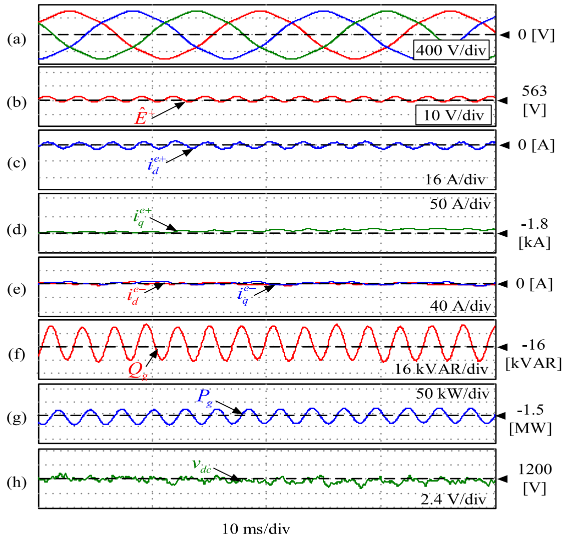

Fig. 20. System performance under distorted grid conditions using proposed method. (a) Grid voltages (V). (b) $\hat{E}^+$(V). (c) Positive-sequence d-axis grid current component (A). (d) Positive-sequence q-axis grid current component (A). (e) Negative-sequence grid current components (A). (f) Grid-side reactive power (VAR). (g) Grid-side active power (W). (h) DC-link voltage (V).

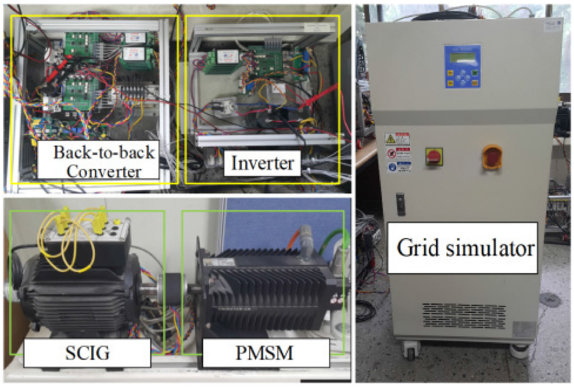

Fig. 21. Schematic diagram of the experimental system.

VI. EXPERIMENTAL RESULTS

The feasibility of the proposed method is verified through an experimental system built in the laboratory shown in Fig. 21. The SCIG is coupled with a permanent magnet synchronous machine (PMSM), which is set as wind turbine simulator with a power rating of 2.5 kW and operating speed ranging from 550 to 1220 r/min. The grid voltage is 220 V/60 Hz. The dc-link voltage is controlled at 340 V. A 10-kVA grid simulator is used to produce adverse grid conditions. The switching frequency is 4 kHz. The dual eSOGI-FLL parameters were selected as follows, based on the aforementioned procedure: $k_{\text{normal}} = 1$; $k_{\text{fault}} = 6$; $g_{\text{fault}} = -9$; $\delta = 4100$; and $\eta_\omega = 4500$.

Fig. 22 illustrates the system performance under 80% balanced sag using the dual SOGI-FLL-based synchronization method. Fig. 22(a) shows the grid-phase voltages with $\hat{E}^+$observed in Fig. 22(b). The estimated grid frequency is shown in Fig. 22(c). Fig. 22(d)–(f) shows the grid currents, i.e., i_d^{e+}, i_q^{e+}, i_d^{e-}, and i_q^{e-}. The grid-side reactive and active powers

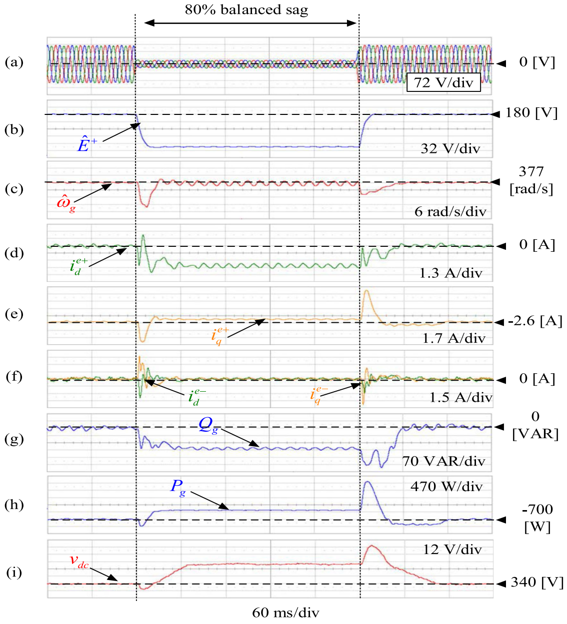

Fig. 22. System performance under 80% balanced sag using dual SOGI-FLL-based synchronization method. (a) Grid voltages (V). (b) $\hat{E}^+$(V). (c) $\hat{\omega}_g$(rad/s). (d) Positive-sequence d-axis grid current component (A). (e) Positive-sequence q-axis grid current component (A). (f) Negative-sequence grid current components (A). (g) Grid-side reactive power (VAr). (h) Grid-side active power (W). (i) DC-link voltage (V).

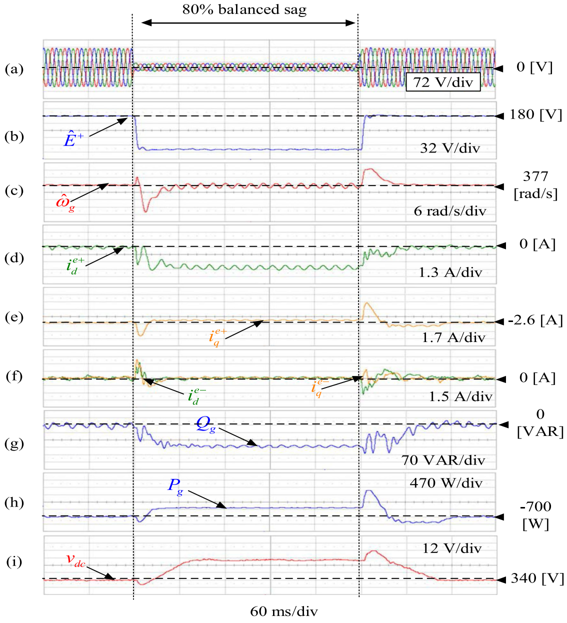

Fig. 23. System performance under 80% balanced sag using proposed method. (a) Grid voltages (V). (b) $\hat{E}^+$(V). (c) $\hat{\omega}_g$(rad/s). (d) Positive-sequence d-axis grid current component (A). (e) Positive-sequence q-axis grid current component (A). (f) Negative-sequence grid current components (A). (g) Grid-side reactive power (VAR). (h) Grid-side active power (W). (i) DC-link voltage (V).

are shown in Fig. 22(g) and (h), respectively. The dc-link voltage is limited to below 374 V (110% of v_{dc}^*) under the voltage sag, as shown in Fig. 22(i).

The system performance under 80% balanced sag using the proposed method is shown in Fig. 23. Similar to the simulation results, it can be observed that the proposed method can offer lower current fluctuations (4.9 A for Δi_q^{e+}, 4.5 A for Δi_d^{e-}, and 4.9 A for Δi_q^{e-}) compared with those using the dual SOGI-FLL-based method, using which $\Delta i_q^{e+}$is 7.65 A, $\Delta i_d^{e-}$is 6 A, and $\Delta i_q^{e-}$is 7.5 A. Moreover, after fault clearance, $\Delta P_{g(\mathrm{clear})}$ and $\Delta v_{\mathrm{dc(clear)}}$ using the proposed method are 2.1 kW and 48 V as shown in Fig. 23(h) and (i), respectively. In contrast, they are 2.8 kW and 61 V using the dual SOGI-FLL-based method as shown in Fig. 22(h) and (i), respectively. It is noted that due to the non-ideal grid voltages with offset components, the fundamental frequency ripples exist in the waveforms.

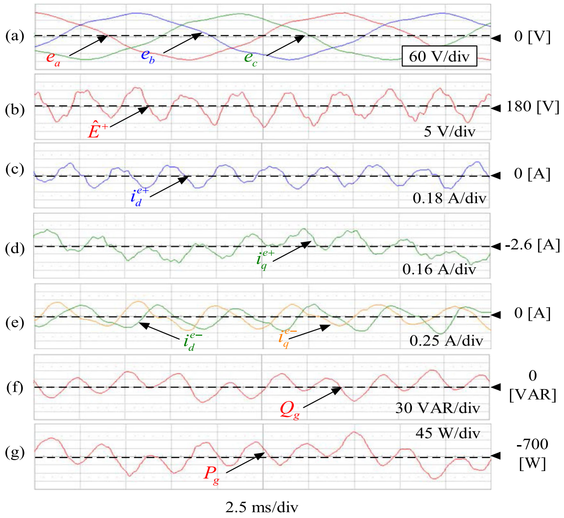

Fig. 24. System performance under distorted grid conditions using dual mSOGI-mFLL-based synchronization method. (a) Grid voltages (V). (b) $\hat{E}^+$(V). (c) Positive-sequence d-axis grid current component (A). (d) Positive-sequence q-axis grid current component (A). (e) Negative-sequence grid current components (A). (f) Grid-side reactive power (VAr). (g) Grid-side active power (W).

Fig. 24 shows the system performance under distorted grid conditions using the dual mSOGI-mFLL-based synchronization method, assuming 4% fifth-order harmonics. The grid-phase voltages are shown in Fig. 24(a). Fig. 24(b) illustrates $\hat{E}^+$ with an average value of 180 V. Due to fifth-order harmonics of the grid voltage, the sixth-order harmonics exist in i_d^{e+}, i_q^{e+}in Fig. 24(c) and (d), and fourth-order harmonics exist in i_d^{e-}, i_q^{e-}in Fig. 24(e). Fig. 24(f) and (g) shows the grid-side reactive and active powers, respectively.

The system performance under distorted grid conditions, in which the 4% fifth-order harmonics are included in the grid-phase voltages, using the proposed method is shown in Fig. 25. In Fig. 25(c)–(e), Δi_d^{e+}, Δi_q^{e+}, Δi_d^{e-}, and Δi_q^{e-} are 0.36, 0.4 0.48, and 0.5 A, respectively. Similar to the simulation results, these current fluctuations are lower than those observed when using the dual mSOGI-mFLL-based method, i.e., 0.54 A for Δi_d^{e+}, 0.64 A for Δi_q^{e+}, 0.83 A for Δi_d^{e-}, and 0.75 A for Δi_q^{e-} shown in Fig. 24(c)–(e). Consequently, the proposed method can offer lower active power fluctuations [156 W for ΔP_g shown in Fig. 25(g)] compared with those observed when using the dual mSOGI-mFLL-based method [250 W for ΔP_g shown in Fig. 24(g)].

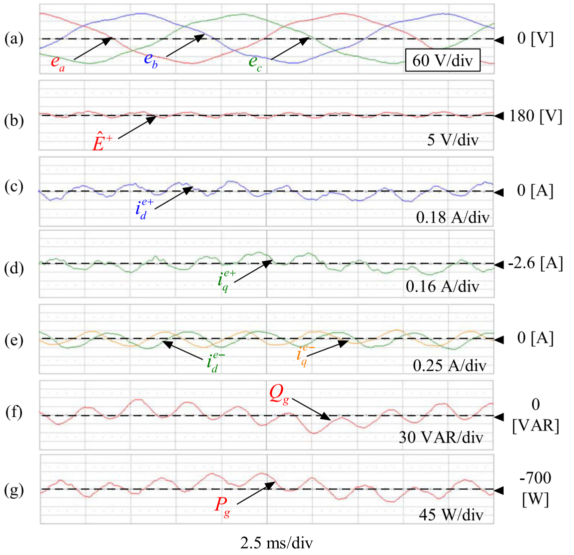

Fig. 25. System performance under distorted grid conditions using proposed method. (a) Grid voltages (V). (b) $\hat{E}^+$(V). (c) Positive-sequence d-axis grid current component (A). (d) Positive-sequence q-axis grid current component (A). (e) Negative-sequence grid current components (A). (f) Grid-side reactive power (VAr). (g) Grid-side active power (W).

VII. CONCLUSION

Based on dual eSOGI-FLL, a novel grid synchronization scheme for three-phase grid-connected converter systems has been proposed in this article. The combination of a dual eSOGI structure with adjustable gains and an FLL with frequency rate limits can accurately estimate the grid voltage even under grid faults. The selection procedure for the dual eSOGI-FLL parameters has been described as well. Through the simulation for a 2-MW SCIG wind turbine system, it is shown that, under 80% balanced sags, the power fluctuations with the proposed method (1.73 MW for $\Delta P_{g(\text{clear})}$ and 1.59 MVAR for $\Delta Q_{g(\text{clear})}$) are lower than those with the dual SOGI-FLL-based synchronization method (2.61 MW for $\Delta P_{g(\text{clear})}$ and 2.22 MVAR for $\Delta Q_{g(\text{clear})}$). In addition, under distorted grid conditions, ΔP_g of 60.3 kW has been observed with the proposed method. In contrast, it is 140.2 kW with the dual mSOGI-mFLL-based synchronization method. The feasibility of the proposed method has been demonstrated through the experimental implementation of a 2.5-kW wind turbine simulator as well.

REFERENCES

[1] S. Chung, "A phase tracking system for three phase utility interface inverters," *IEEE Trans. Power Electron.*, vol. 15, no. 3, pp. 431–438, May 2000.

[2] V. Kaura and V. Blasko, "Operation of phase loop system under distorted utility conditions," *IEEE Trans. Ind. Appl.*, vol. 33, no. 1, pp. 58–63, 1997.

[3] I. Carugati, S. Maestri, P. G. Donato, D. Carrica, and M. Benedetti, "Variable sampling period filter PLL for distorted three-phase systems," *IEEE Trans. Power Electron.*, vol. 27, no. 1, pp. 321–330, Jan. 2012.

[4] S. Golestan, J. M. Guerrero, and A. M. Abusorrah, "MAF-PLL with phase-lead compensator," *IEEE Trans. Ind. Electron.*, vol. 62, no. 6, pp. 3691–3695, Jun. 2015.

[5] L. Hadjidemetriou, Y. Yang, E. Kyriakides, and F. Blaabjerg, "A synchronization scheme for single-phase grid-tied inverters under harmonic distortion and grid disturbances," *IEEE Trans. Power Electron.*, vol. 32, no. 4, pp. 2784–2793, Apr. 2017.

[6] M. Karimi-Ghartemani and M. R. Iravani, "A method for synchronization of power electronic converters in polluted and variable-frequency environments," *IEEE Trans. Power Syst.*, vol. 19, no. 3, pp. 1263–1270, Aug. 2004.

[7] D. Yazdani, M. Mojiri, A. Bakhshai, and G. Joos, "A fast and accurate synchronization technique for extraction of symmetrical components," *IEEE Trans. Power Electron.*, vol. 24, no. 3, pp. 674–684, Mar. 2009.

[8] P. Rodríguez, J. Pou, J. Bergas, J. I. Candela, R. P. Burgos, and D. Boroyevich, "Decoupled double synchronous reference frame PLL for power converters control," *IEEE Trans. Power Electron.*, vol. 22, no. 2, pp. 584–592, Mar. 2007.

[9] F. D. Freijedo, J. Doval-Gandoy, O. Lopez, and E. Acha, "A generic open-loop algorithm for three-phase grid voltage/current synchronization with particular reference to phase, frequency, and amplitude estimation," *IEEE Trans. Power Electron.*, vol. 24, no. 1, pp. 94–107, Jan. 2009.

[10] E. Robles, S. Ceballos, J. Pou, J. Mart´ın, J. Zaragoza, and P. Ibañez, "Variable-frequency grid-sequence detector based on a quasi-ideal lowpass filter stage and a phase-locked loop," *IEEE Trans. Power Electron.*, vol. 25, no. 10, pp. 2552–2563, Oct. 2010.

[11] H. Yi, X. Wang, F. Blaabjerg, and F. Zhuo, "Impedance analysis of SOGI-FLL-based grid synchronization," *IEEE Trans. Power Electron.*, vol. 32, no. 10, pp. 7409–7413, Oct. 2017.

[12] J. Yu, W. Shi, J. Li, L. Deng, and M. Pei, "A discrete-time non-adaptive SOGI-based frequency-locked loop," *IEEE Trans. Power Syst.*, vol. 35, no. 6, pp. 4912–4915, Nov. 2020.

[13] J. Matas, H. Martín, J. de la Hoz, A. Abusorrah, Y. Al-Turki, and H. Alshaeikh, "A new THD measurement method with small computational burden using a SOGI-FLL grid monitoring system," *IEEE Trans. Power Electron.*, vol. 35, no. 6, pp. 5797–5811, Jun. 2020.

[14] W. Xu, Y. Jiang, C. Mu, and F. Blaabjerg, "Improved nonlinear flux observer-based second-order SOIFO for PMSM sensorless control," *IEEE Trans. Power Electron.*, vol. 34, no. 1, pp. 565–579, Jan. 2019.

[15] A. T. Nguyen and D.-C. Lee, "Sensorless control of DFIG wind turbine systems based on SOGI and rotor position correction," *IEEE Trans. Power Electron.*, vol. 36, no. 5, pp. 5486–5495, May 2021.

[16] J. Matas, M. Castilla, J. Miret, L. G. De Vicuña, and R. Guzman, "An adaptive prefiltering method to improve the speed /accuracy trade-off of voltage sequence detection methods under adverse grid conditions," *IEEE Trans. Ind. Electron.*, vol. 61, no. 5, pp. 2139–2151, May 2014.

[17] P. Rodríguez, A. Luna, I. Candela, R. Mujal, R. Teodorescu, and F. Blaabjerg, "Multiresonant frequency-locked loop for grid synchronization of power converters under distorted grid conditions," *IEEE Trans. Ind. Electron.*, vol. 58, no. 1, pp. 127–138, Jan. 2011.

[18] P. Rodríguez, A. Luna, R. S. Muñoz-Aguilar, I. Etxeberria-Otadui, R. Teodorescu, and F. Blaabjerg, "A stationary reference frame grid synchronization system for three-phase grid-connected power converters under adverse grid conditions," *IEEE Trans. Power Electron.*, vol. 27, no. 1, pp. 99–112, Jan. 2012.

[19] T. Bei and P. Wang, "Robust frequency-locked loop algorithm for grid synchronisation of single-phase applications under distorted grid conditions," *IET Gener., Transmiss., Distrib.*, vol. 10, no. 11, pp. 2593–2600, Aug. 2016.

[20] M. S. Reza, M. Ciobotaru, and V. G. Agelidis, "Accurate estimation of single-phase grid voltage fundamental amplitude and frequency by using a frequency adaptive linear Kalman filter," *IEEE J. Emerg. Sel. Topics Power Electron.*, vol. 4, no. 4, pp. 1226–1235, Dec. 2016.

[21] S. Golestan, J. M. Guerrero, J. C. Vasquez, A. M. Abusorrah, and Y. A. Al-Turki, "Single-phase FLLs based on linear Kalman filter, limit-cycle oscillator, and complex bandpass filter: Analysis and comparison with a standard FLL in grid applications," *IEEE Trans. Power Electron.*, vol. 34, no. 12, pp. 11774–11790, Dec. 2019.

[22] C. M. Hackl and M. Landerer, "Modified second-order generalized integrators with modified frequency locked loop for fast harmonics estimation of distorted single-phase signals," *IEEE Trans. Power Electron.*, vol. 35, no. 3, pp. 3298–3309, Mar. 2020.

[23] X. He, H. Geng, and G. Yang, "A generalized design framework of notch filter based frequency-locked loop for three-phase grid voltage," *IEEE Trans. Ind. Electron.*, vol. 65, no. 9, pp. 7072–7084, Sep. 2018.

[24] M. Mojiri, M. Karimi-Ghartemani, and A. Bakhshai, "Time-domain signal analysis using adaptive notch filter," *IEEE Trans. Signal Process.*, vol. 55, no. 1, pp. 85–93, Jan. 2007.

[25] J.-S. Park, T. H. Nguyen, and D.-C. Lee, "Advanced SOGI-FLL scheme based on fuzzy logic for single-phase grid-connected converters," *J. Power Electron.*, vol. 14, no. 3, pp. 598–607, May 2014.

[26] A. T. Nguyen and D.-C. Lee, “Advanced LVRT strategy for SCIG-based wind energy conversion systems using feedback linearization and sliding mode control,” *J. Power Electron.*, vol. 21, no. 8, pp. 1180–1189, 2021.

[27] Z. Xin, E. Zhao, F. Blaabjerg, L. Zhang, and P. C. Loh, “An improved flux observer for field-oriented control of induction motors based on dual second-order generalized integrator frequency-locked loop,” *IEEE J. Emerg. Sel. Topics Power Electron.*, vol. 5, no. 1, pp. 513–525, Mar. 2017.

[28] X. Luo *et al.*, “Review of voltage and frequency grid code specifications for electrical energy storage applications,” *Energies*, vol. 11, no. 5, Apr. 2018, Art. no. 1070.

[29] J. Svensson, M. Bongiorno, and A. Sannino, “Practical implementation of delayed signal cancellation method for phase-sequence separation,” *IEEE Trans. Power Del.*, vol. 22, no. 1, pp. 18–26, Jan. 2007.

[30] H.-S. Song and K. Nam, “Dual current control scheme for PWM converter under unbalanced input voltage conditions,” *IEEE Trans. Ind. Electron.*, vol. 46, no. 5, pp. 953–959, Oct. 1999.

[31] M. Tsili and S. Papathanassiou, “A review of grid code technical requirements for wind farms,” *IET Renewable Power Gener.*, vol. 3, no. 3, pp. 308–332, Sep. 2009.

[32] K. Shi, T. Li, M. Ren, and P. Xu,, “Low voltage ride–through control strategy for virtual synchronous generators based on virtual self–inductive fux linkage,” *J. Power Electron.,* vol. 21, no. 5, pp. 815–828, May 2021.

Anh Tan Nguyen (Member, IEEE) received the B.S. degree from the Hanoi University of Science and Technology, Hanoi, Vietnam, in 2014, and the Ph.D. degree from Yeungnam University, Gyeongsan, South Korea, in 2021, both in electrical engineering.

He was a Postdoctoral Fellow with the Department of Electrical Engineering, Yeungnam University, Gyeongsan, South Korea, from August to November 2021. Since 2022, he has been a Faculty Member with the School of Electrical Engineering, Hanoi University of Science and Technology, Hanoi, Vietnam, and was the Secretary of Vietnam Power Electronics Community. His current research interests include machine drives, grid-connected converter control, and wind energy conversion systems.

Dong-Choon Lee (Senior Member, IEEE) received the B.S., M.S., and Ph.D. degrees in electrical engineering from Seoul National University, Seoul, South Korea, in 1985, 1987, and 1993, respectively.

He was a Research Engineer for Daewoo Heavy Industry, South Korea, from 1987 to 1988. Since 1994, he has been a Faculty Member with the Department of Electrical Engineering, Yeungnam University, Gyeongsan, South Korea,. He was a Visiting Scholar with Power Quality Laboratory, Texas A&M University, College Station, TX, USA, in 1998; the Electrical Drive Center, University of Nottingham, Nottingham, U.K., in 2001; the Wisconsin Electric Machines and Power Electronics Consortium, University of Wisconsin, Madison, WI, USA, in 2004; and the FREEDM Systems Center, North Carolina State University, Raleigh, NC, USA, from September 2011 to August 2012. His current research interests include power converter design and control, renewable energy and its grid connection, ac machine drives, and dc power system.

Dr. Lee is currently an Associate Editor for the IEEE TRANSACTIONS ON POWER ELECTRONICS and an RDL of IEEE PELS. He was the Editor-in-Chief for the *Journal of Power Electronics* of the Korean Institute of Power Electronics (KIPE), from January 2015 to December 2017. In 2019, he was the President of KIPE.